# Broad Dual-band Metamaterial Filter with Sharp Out-of-band Rejections

**Limei Qi[1,2]\* and Syed Mohsin Ali Shah[1]**

[1]*School of Electronic Engineering, Beijing University of Posts and Telecommunications,
Beijing 100876, China*
[2]*State Key Laboratory of Millimeter Waves, Southeast University, Nanjing 210096 China*

A broad dual-band terahertz metamaterial filter with sharp out-of-band rejections is designed and demonstrated. The center frequencies of the first and the second bands occur at 0.35 THz and 0.96 THz with 3 dB relative bandwidth of 31% and 17%, respectively. Results are measured using a THz time-domain spectroscopy system that shows agreement with simulations. Physical mechanisms of the broad dual-band resonance are clarified based on transmissions of different structures and surface current density distributions. Influence of structure parameters on the transmission characteristics are discussed. Symmetry of the structure ensures the filter polarization independence at normal incidence. These results supported by the design of the filter could find applications in broad multi-band sensors, terahertz communication systems, and other emerging terahertz technologies.

*Keywords* : Metamaterial, Terahertz, Filter, Dual band
*OCIS codes* : (300.6495) Spectroscopy, terahertz; (160.3918) Metamaterials; (230.7408) Wavelength
filtering devices

## I. INTRODUCTION

Terahertz (THz) techniques have received considerable attention during the past decades [1, 2]. Metamaterials are considered as competent candidates for terahertz devices due to their strong magnetic or electric responses at terahertz frequencies [3-6]. Metamaterial bandpass filters are important terahertz devices and can be used in spectroscopy, security, imaging, and sensing [7-9]. Recently, narrow [10-12] and broadband [13, 14] terahertz metamaterial filters with single-band resonance have been designed and fabricated. In THz communication systems, to obtain even greater increases in communications capacity, filters with multiple broad bands are needed [15, 16]. A metal-dielectric filter consisting of two different four-legged loaded slots showed two narrow pass bands at 0.183 and 0.22 THz [17]. A dual-band filter consisting of metal-dielectric-metal sandwich structure was simulated, and two pass bands centered at 0.97 THz and 1.37 THz have a transmission of 90% [18]. A photonic crystal dual-mode dual-band terahertz filter was

designed and formed by a point defect micro cavity [19]. A metal-dielectric-metal filter consisting of a periodic square close ring array exhibited the multiband transmission with low average insertion loss, steep skirts and high out-of-band rejection [20]. For the dual-band or multi-band filters reported above [17-20], no further experimental demonstration was carried out.

Recently, through depositing identical four-split complementary layers on both sides of a quartz crystal, Lu *et al.* [21] measured a dual-band filter with the fundamental band ranging from 0.227 THz to 0.283 THz and the second band occurring between 0.59 THz and 0.68 THz [21]. Lan *et al.* [22] proposed a dual-resonance band pass filter using a modified four-split metal-dielectric-metal structure to improve the transmission performance. The measured dual bands centered at 0.315 THz and 0.48 THz were in good agreement with the simulations. Based on metal-dielectric structure, Qi *et al.* [23] proposed multi-band filters which were insensitive to any polarization due to the symmetry of concentric rings [23]. They also fabricated terahertz

*Corresponding author: qilimei1204@163.com, ORCID 0000-0003-0449-4733

Color versions of one or more of the figures in this paper are available online.

dual-band filters using laser perforation of a periodic array of air slots in molybdenum, and achieved good selectivity performance both in the lower and higher bands [24].

For the fabricated multi-band or dual-band filters reported above, the bandwidths are usually very narrow [23, 24], or only the fundamental band is wide while the second one is relatively narrow [22] and the out-of-band rejection is not sharp [21]. In this paper, a broad dual-band terahertz filter with sharp out-of-band rejections is presented using two identical four-split complementary electric inductive-capacitive (CELC) metal layers on each side of the dielectric substrate. Results measured using a THz time-domain spectroscopy system are consistent with simulations. The simulated center frequencies occur at 0.35 THz and 0.96 THz with the 3 dB relative bandwidth of 31% and 17%, which are much wider than the structure in [22] where the 3 dB relative bandwidth is only 10% and 1% for the first and the second bands, respectively. At the same time, sharp out-of-band rejections are obtained in the two bands compared with other broadband terahertz filters [21, 22]. Finally, effects of structure parameters on transmission characteristics of the dual-band filter are discussed.

## II. METHODS AND RESULTS

Figs. 1(a) and 1(b) show the top and side views of the unit cell, respectively, which consists of three layers. The identical metallic fourfold rotational symmetry layers are deposited on the upper and lower sides of the dielectric substrate. Unit cell of the structure has dimensions $P = 150$, $R = 70$, $W = 13$, $h = 120$ (all sizes in μm). Aluminum with a conductivity of $\sigma = 3.72 \times 10^7$ S/m and thickness of 200 nm is used as the metal layer, and the dielectric material is a crystal quartz with the relative permittivity $\varepsilon_r = 4.41$ and the loss tangent $tg\delta = 0.0004$ [26]. The sample was fabricated using standard photolithographic techniques and the microscope images at scale 50 μm and 100 μm are shown in Figs. 1(c) and 1(d), respectively. In the simulation, periodic boundary conditions are set along the x and y axes with open (add space) boundary in the z axis, then the wave ports are automatically added in the z axis of normal incidence to the structure. Due to the symmetrical design of the unit cell, the transverse electric (TE) polarization and the transverse magnetic (TM) polarization have the same transmission frequency response under normal incidence.

Terahertz time-domain-spectroscopy was used to characterize the dual-band responses. Figure 2 shows the transmission of the filter at normal incidence, where the solid and dashed lines denote the measurement and simulation, respectively. Inspection of the transmission curves clearly indicates that a broad and dual-band filter is achieved at the center frequencies of 0.35 THz and 0.96 THz. In the simulation, the first band appears between the two resonance frequencies $f_1 = 0.311$ THz and $f_2 = 0.383$ THz. The second band appears between the two resonance frequencies $f_3 = 0.898$ THz and $f_4 = 1.019$ THz. The 3 dB relative bandwidths of the first and the second band are 31% and 17%, respectively. The measured transmission matches the simulation except for the slight shift and the
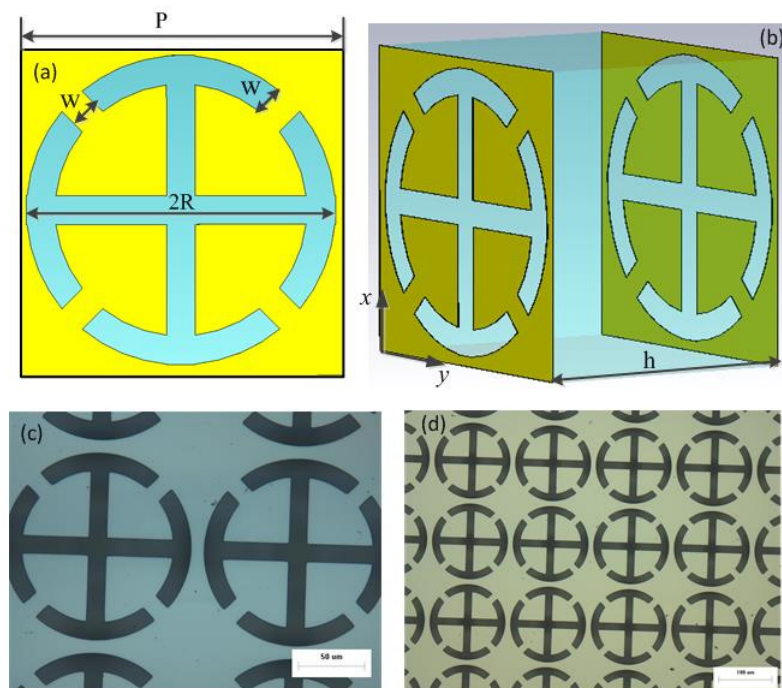


FIG. 1. Schematic view of the fourfold rotational symmetry filter, where P = 150, R = 70, W = 13, and h = 120 (all sizes in μm). (a) top view, (b) side view, microscope images of the fabricated sample at scale (c) 50 μm and (d) 100 μm.
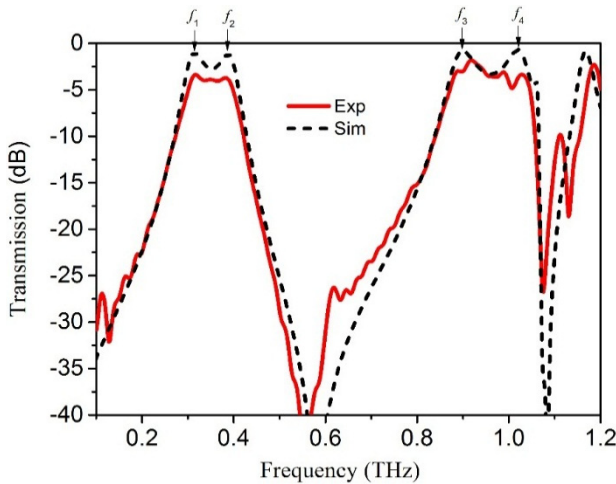
FIG. 2. The measured (solid line) and simulated (dash line) transmission curves for the broad dual-band filter at normal incidence.



FIG. 3. Influence of (a) metal material and (b) dielectric loss on the transmission.

larger insertion loss in the measurement. The slight shift may be attributed to the deviation of fabrication. As for the insertion loss in the experiment, the increment value is 3.87 dB and 4.0 dB for the first and the second bands, respectively, compared with the simulations. Figure 3 shows the effect of metal conductivity and dielectric loss tangent tgδ on the transmission. In Fig. 3(a), the dashed, solid and dot-dashed lines correspond to the results of aluminum with $\sigma = 3.72 \times 10^7$ S/m, gold with $\sigma = 4.56 \times 10^7$ S/m, and copper with $\sigma = 5.96 \times 10^7$ S/m, respectively. It is clearly seen that the transmissions are nearly the same due to little difference in the conductivities. In Fig. 3(b), the transmissions are overlapped for the dielectric loss of tgδ = 0 and 0.0004. An increment value of 0.34 dB and 1 dB occurs until tgδ increases to 0.02. Therefore, changing metal material and introducing low-loss quartz have little effect on insert loss in the pass bands. The large loss in the experiment may be caused by water vapor and moisture since the waves in the terahertz band are sensitive to them.

To investigate the origin of the two broad bands, Fig. 4 shows the transmission of the dielectric only (D, dot line), metal-dielectric structure (MD, dot-dashed line), and metal-dielectric-metal structure (MDM, solid line). The parameters are same as those in Fig. 1. For the dielectric only, the transmission (dotted line in Fig. 4.) changes periodically with interval of 0.6 THz due to the Fabry-Perot effect. The frequency interval of the Fabry-Perot resonance can be described by the formula below [25, 27]:

$$\Delta f = \frac{c}{2nh\cos\theta} \tag{1}$$

where $n = 2.1$ is the index of the quartz crystal, $h = 120$ μm is the height of the quartz, and θ is the THz incident angle. For normal incidence, $\triangle f = 0.595$ THz, $2\triangle f = 1.19$ correspond to the resonances of the dielectric. When a
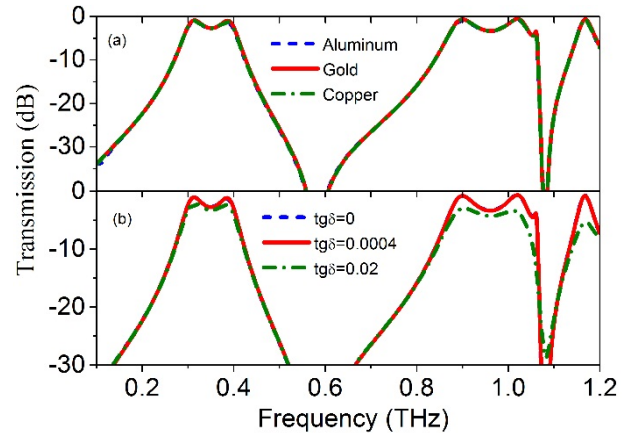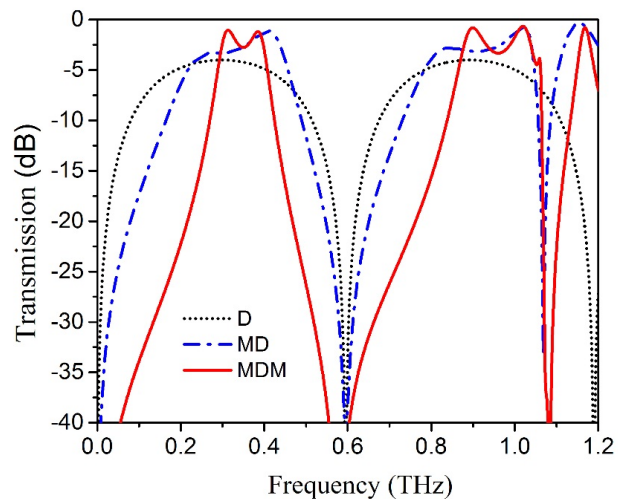


FIG. 4. Transmission for the dielectric only (dotted line), single metal-dielectric structure (MD, dot-dashed line) and metal-dielectric-metal structure (MDM, solid line). The parameters are same as those in Fig. 1.

single-layer metal is put on one side of the quartz crystal, both the transmission magnitude and the out-of-band resistance increase. The excitation of the surface plasmons by the periodically arranged metal arrays in the MD structure is considered to be responsible for this resonant effect [13]. When two metal layers are put on each side of the quartz crystal, the resonance modes around each interface start to interact and couple together and then give rise to the higher transmission, narrower bandwidth and sharper out-of-band resistance.

To give more insight of the coupling of the two metal layers in the dual-band filters, Fig. 5 shows surface current distributions of the two pass bands at the top and bottom layers. The yellow parts indicate the metallic Al layers, red lines with arrows indicate instantaneous directions of the current flow and their lengths correspond to the current lengths. Figs. 5(a) and 5(b) show surface current distributions
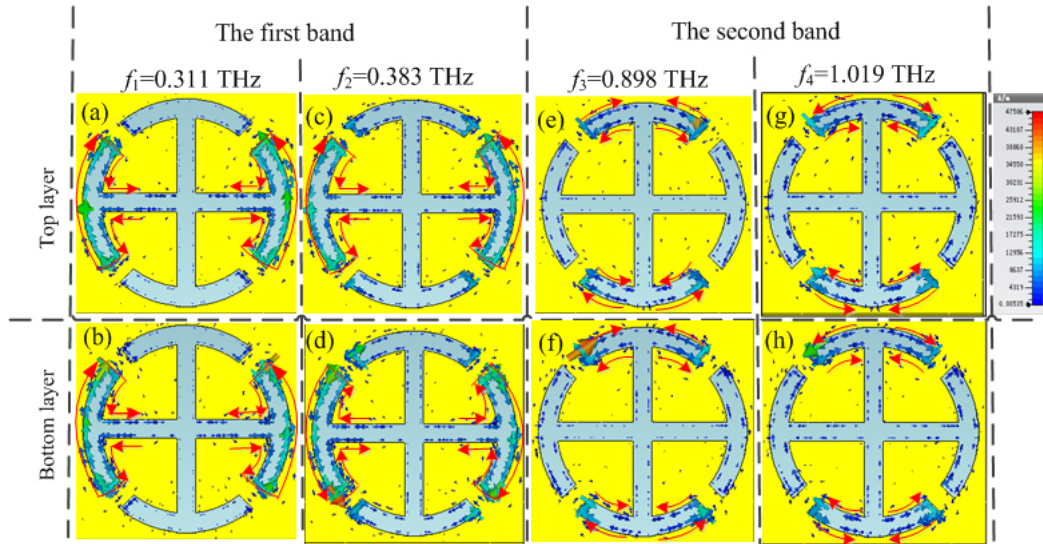
FIG. 5. Surface current density distributions of the two pass bands. The yellow parts indicate the metallic Al layers, red lines with arrows indicate instantaneous directions of the current flow. (a) The top layer and (b) bottom layer of $f_1 = 0.311$ THz. (c) The top layer and (d) bottom layer of $f_2 = 0.383$ THz. (e) The top layer and (f) bottom layer of $f_3 = 0.898$ THz. (g) The top layer and (h) bottom layer of $f_4 = 1.019$ THz.

of the top and bottom layer at $f_1 = 0.311$ THz in the first band. Figs. 5(c) and 5(d) show surface current distributions of the top and bottom layer at $f_2 = 0.383$ THz in the first band. At the first resonance $f_1 = 0.311$ THz, a symmetric mode exists between the top and bottom layers, resulting in an electric resonance. At the second resonance $f_2 = 0.383$ THz, an anti-symmetric mode exists between the top and bottom layers, resulting in a magnetic dipolar resonance. The induced currents interact with each other to equate to a "trapped-mode resonance" [28-30] and then give rise to a broadband pass filter in the THz region. Figs. 5(e) and 5(f) show surface current distributions of the top and bottom layers at $f_3 = 0.898$ THz in the second band. Figs. 5(g) and 5(h) show surface current distributions of the top and bottom layers at $f_4 = 1.019$ THz in the second band. It is seen that the second broadband filter appears due to the symmetric induced currents between the top and bottom layers at the two resonance modes.

Figure 6 shows influence of period P and radius R on the transmittance spectra. In Fig. 6(a), parameters of R = 70 μm, W = 13 μm, h = 120 μm remain unchanged. It is seen that as period P increases from 145 μm to 155 μm, bandwidths of the two bands decrease because the relative air holes become smaller in one unit cell and may allow little waves to transmit through them. At the same time, the out-of-band rejection decreases from 47 dB to 22 dB at the higher frequency of the second band. As period P increases to 165 μm, the out-of-band rejection of the second band decreases to 11 dB with the dip transmission increasing to 6.8 dB. In Fig. 6(b) when radius R increases from 62.5 μm to 72.5 μm with the parameters P = 150 μm, W = 13 μm and h = 120 μm unchanged, the two bands shift to the lower frequency because the center

frequency is inversely proportional to the air holes of the structure [31]. For the first band, both the bandwidth and magnitude change a little, while they increase in the second band. The out-of-band rejections at the higher frequency of the two bands increase with increasing radius.

Figure 7 shows the transmittance spectra under various width w and substrate thickness h. In Fig. 7(a), as w varies from 11 μm to 17 μm with P = 150 μm, R = 70 μm, h = 120 μm fixed, bandwidth of the first band increases while it decreases for the second band. The out-of-band rejections decrease at the higher frequencies of the two pass bands. Different from the change of period P, increasing width w allows more waves to transmit through the air holes and the bandwidth of the two pass bands increases as well as the magnitude. In Fig. 7(b), parameters
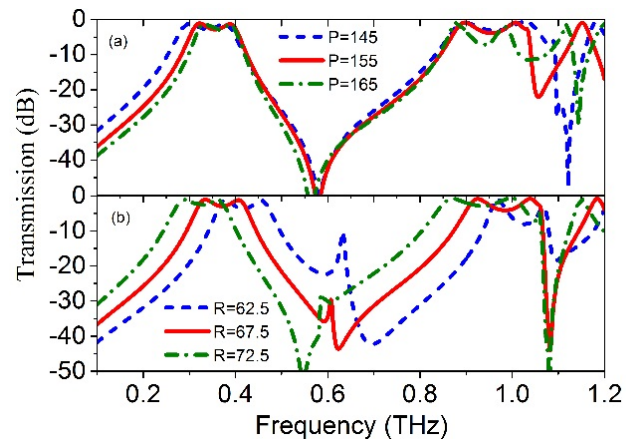


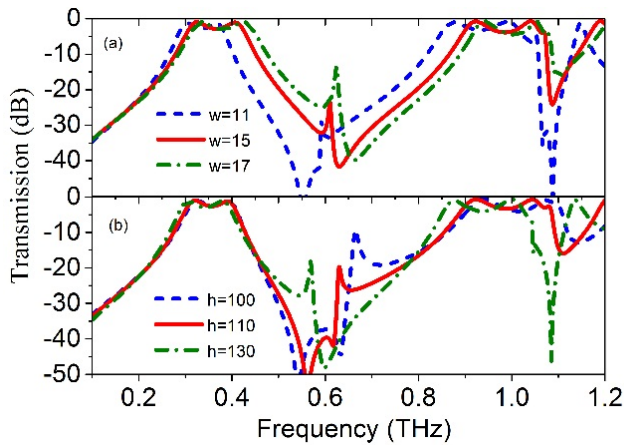FIG. 6. Transmission for different period and radius (a) period P, and (b) radius R.

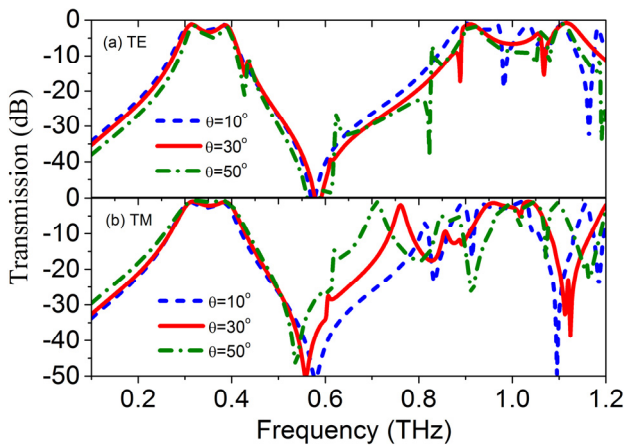FIG. 7. Transmission for different width and substrate thickness (a) width w, and (b) substrate thickness h.



FIG. 8. Transmission of oblique incidence for (a) TE and (b) TM polarization.

of P = 150 μm, R = 70 μm, W = 13 μm remain unchanged. As substrate thickness h increases from 100 μm to 130 μm, the first band has little change. For the second band, the right side of the pass band shifts to the lower frequency with the out-of-band rejections increasing. Moreover, an obvious shift of spurious resonance is seen around 0.6 THz and 1.15 THz in Fig. 7(b). It is calculated that the frequency intervals of the Fabry-Perot are △f = 0.714, 0.649 and 0.549 THz for h = 100, 110 and 130 μm, respectively, which correspond to the results with the dashed, solid and dot-dashed lines near 0.6 THz. The second order of the Fabry-Perot frequency intervals are 2△f = 1.428, 1.298 and 1.1 THz. The peak near 1.15 THz for h = 130 μm is only shown with the dot-dashed line. As the Fabry-Perot resonance is dependent on the thickness and permittivity of the dielectric, the Fabry-Perot resonances in Figs. 6(b) and 7(a) have little change while increasing the radius or width.

For the structure with dimensions P = 150, R = 70, W = 13, h = 120 (all sizes in μm), Fig. 8 shows the transmission magnitude of the TE (the electric field is parallel to the x-axis) and TM polarizations (the electric field is parallel to the y-axis) under different incidence angles. As angles increase from 0° to 50°, location and bandwidth slightly change for the first band, while the pass property of the second band disappears. The results confirm that location and bandwidth of the first band are nearly independent of incidence angles, while the second band is sensitive to incidence angles and it can hardly be used as a filter under oblique incidence. The sharp resonant peaks around △f = 0.604, 0.633 and 0.687 THz are also caused by the Fabry-Perot resonance under the oblique incident angles θ = 10°, 20° and 30°, respectively. For the parasitic oscillations around the second band, they may be due to the multiple scattering of oblique incidence.

## III. CONCLUSION

In summary, we demonstrated a broad and dual-band filter centered at 0.35 THz and 0.96 THz. The filter is polarization independent at normal incidence due to its fourfold rotation symmetry. The measured transmission matches the simulation except the slight shift and the larger insertion loss occurring in the measured result. The shift may be caused by the dimension error processing and the finite size of fabricated filter. The larger loss is mainly introduced by the finite conductivity of the metal film and the larger dielectric loss in the substrate at the higher frequencies. Influences of filter parameters on the transmission spectra are investigated. As period increases, bandwidths of the two bands and the out-of-band rejection of the second band decrease. As radius increases, the two bands shift to the lower frequency with the out-of-band rejection increasing to the higher frequency. As width increases, bandwidth of the first band increases while it decreases for the second band. As substrate thickness increases, the first band changes a little, while the second band shifts to the lower frequency with out-of-band rejections increasing on both sides. Under oblique incidence, the first band is nearly independent of the incidence angle, while the second band may be divided into some narrow pass bands and can't be used as band pass filter under large oblique incident angles.

## REFERENCES

1. D. M. Mittlemana, "Perspective: terahertz science and technology," J. Appl. Phys. **122**, 230901 (2017).
2. Q. Sun, Y. He, K. Liu, S. Fan, E. P. J. Parrott, and E. Pickwell-Mac. Pherson, "Recent advances in terahertz technology for biomedical applications," Quant. Imaging Med. Surg. **7**, 345-355 (2017).
3. T. J. Yen, W. J. Padilla, N. Fang, D. C. Vier, D. C. Smith, J. B. Pendry, D. N. Basov, and X. Zhang, "Terahertz magnetic response from artificial materials," Science **303**, 1491-1496, 2004.
4. F. Ling, Z. Zhong, R. Huang, and B. Zhang, "A broadband tunable terahertz negative refractive index metamaterial," Sci. Rep. **8**, 9843 (2018).
5. H. Chen, W. J. Padilla, J. M. O. Zide, A. C. Gossard, A. J. Taylor, and R. D. Averitt, "Active metamaterial terahertz devices," Nature **444**, 597-600 (2006).
6. Z. Huang, Q. Han, C. Ji, J. Wang, and Y. Jiang "Broadband terahertz modulator based on graphene metamaterials," AIP Adv. **8**, 035304 (2018).
7. Y. Demirhan, H. Alaboz, M. A. Nebioğlu, B. Mulla, M. Akkaya, H. Altan, C. Sabah, and L. Ozyuzer, "Fourcross shaped metamaterial filters fabricated from high temperature superconducting YBCO and Au thin films for terahertz waves," Supercond. Sci. Technol. **30**, 074006 (2017).
8. X. Zhang, J. Gu, W. Cao, J. Han, A. Lakhtakia, and W. Zhang, "Bilayer-fish-scale ultrabroad terahertz bandpass filter," Opt. Lett. **37**, 906-908 (2012).
9. L. Wang, Z. Geng, X. He, Y. Cao, Y. Yang, and H. Chen, "Realization of band-pass and low-pass filters on a single chip in terahertz regime," Optoelec. Lett. **11**, 33-35 (2015).
10. A. K. Azad, Y. Zhao, W. Zhang, and M. He, "Effect of dielectricproperties of metals on terahertz transmission subwavelength hole arrays," Opt. Lett. **31**, 2637-2639 (2006).
11. X. Lu, J. Han, and W. Zhang, "Resonant terahertz reflection of periodic arrays of subwavelength metallic rectangles," Appl. Phys. Lett. **92**, 121103 (2008).
12. J. Li, "Terahertz wave narrow bandpass filter based on photonic crystal," Opt. Commun. 283, 2647-2650 (2010).
13. J. Han, J. Gu, X. Lu, M. He, Q. Xing, and W. Zhang, "Broadband resonant terahertz transmission in a composite metal-dielectric structure," Opt. Express **17**, 16527-16534 (2009).
14. O. Paul, R. Beigang, and M. Rahm, "Highly selective terahertz bandpass filters based on trapped mode excitation," Opt. Express **17**, 18590-18595 (2009).
15. H. J. Song and T. Nagatsuma, "Present and future of terahertz communications," IEEE Trans. Terahertz Sci. Technol. **1**, 256-263 (2011).
16. T. Kleine-Ostmann and T. Nagatsuma, "A review on terahertz communications research," J. Infrared Millim. Terahertz Waves **32**, 143-171 (2011).
17. C. Guo, H. Sun, and X. Lu, "A novel dual band frequency selective surface with periodic cell perturbation," Prog. Electromagn. Res. B **9**,137-149 (2008).
18. Y. Chiang and T. Yen, "A high-transmission dual band terahertz bandpass filter by exciting multiresonance of metamaterials," Proc. SPIE **8070**, Metamaterials VI, 80700V (2011).
19. O. Karakilinc and M. Dinley, "Design of dual-mode dual-band photonic crystal bandpass filters for terahertz communication applications," Microwave Opt. Technol. Lett. **57**, 1806-1810 (2015).
20. X. Chen and W. Fan, "A multiband THz bandpass filter based on multiple-resonance excitation of a composite metamaterial," Mater. Res. Express **2**, 055801 (2015).
21. M. Lu, W. Li, and E. R. Brown, "Second-order bandpass THz filter achieved by multilayer complementary metamaterial structures," Opt. Lett. **36**, 1071-1073 (2011).
22. F. Lan, Z. Yang, L. Qi, X. Gao, and Z. Shi, "Terahertz dual-resonance bandpass filter using bilayer reformative complementary metamaterial structures," Opt. Lett. **39**, 1709-1712 (2014).
23. L. Qi and C. Li, "Multi-band terahertz filter with independence to polarization and insensitivity to incidence angles," J. Infrared, Millimeter, Terahertz Waves **36**, 1137-1144 (2015).
24. L. Qi, C. Li, G. Fang, and S. Li, "Single-layer dual-band terahertz filter with weak coupling between two neighboring cross slots," Chin. Phys. B **24**, 107802 (2015).
25. H. Chen, J. F. O'Hara, A. J. Taylor, R. D. Averitt, C. Highstrete, M. Lee, and W. J. Padilla, "Complementary planar terahertz metamaterials," Opt. Express **15**, 1084-1095 (2007).
26. X. Liu, D. A. Powell, and A.Alù, "Correcting the Fabry-Perot artifacts in metamaterial retrieval procedures," Phys. Rev. B **84**, 235106 (2011).
27. Z. Zhao, H. Zhao, W. Peng, and W. Shi, "Polarization dependence of terahertz Fabry-Pérot resonance in flexible complementary metamaterials," Plasmonics **10**, 1587-1592 (2015).
28. V. A. Fedotov, M. Rose, S. L. Prosvirnin, N. Papasimakis, and N. I. Zheludev, "Sharp trapped-mode resonances in planar metamaterials with a broken structural symmetry," Phys. Rev. Lett. **99**, 147401 (2007).
29. N. Papasimakis, V. A. Fedotov, N. I. Zheludev, and S. L. Prosvirnin, "Metamaterial analog of electromagnetically induced transparency," Phys. Rev. Lett. **101**, 253903 (2008).
30. T. Yeh, S. Genovesi, A. Monorchio, E. Prati, F. Costa, T. Huang, and T. Yen, "Ultra-broad and sharp-transition bandpass terahertz filters by hybridizing multiple resonances mode in monolithic metamaterials," Opt. Express **20**, 7580-7589 (2012).
31. B. A. Munk, *Frequency Selective Surfaces: Theory and Design, 1st Edn.* (John Wiley and Sons Inc., 2000), pp. 5, 393.